Phase-space structure in the local dark matter distribution and its signature in direct detection experiments

Vogelsberger, Mark; Helmi, Amina; Springel, Volker; White, Simon D. M.; Wang, Jie; Frenk, Carlos S.; Jenkins, Adrian; Ludlow, Aaron; Navarro, Julio F.

Published in:
Monthly Notices of the Royal Astronomical Society

DOI:
10.1111/j.1365-2966.2009.14630.x

Publication date:
2009

Mon. Not. R. Astron. Soc. **395,** 797–811 (2009) doi:10.1111/j.1365-2966.2009.14630.x

Phase-space structure in the local dark matter distribution and its signature in direct detection experiments

Mark Vogelsberger,[1⋆] Amina Helmi,[2] Volker Springel,[1] Simon D. M. White,[1] Jie Wang,[1,3] Carlos S. Frenk,[3] Adrian Jenkins,[3] Aaron Ludlow[2] and Julio F. Navarro[4,5]

[1]*Max-Planck-Institut für Astrophysik, Karl-Schwarzschild-Straße 1, 85740 Garching bei München, Germany*
[2]*Kapteyn Astronomical Institute, University of Groningen, PO Box 800, 9700 AV Groningen, the Netherlands*
[3]*Institute for Computational Cosmology, Department of Physics, University of Durham, South Road, Durham DH1 3LE*
[4]*Department of Physics and Astronomy, University of Victoria, Victoria, BC, V8P 5C2, Canada*
[5]*Department of Astronomy, University of Massachusetts, Amherst, MA 01003-9305, USA*

Accepted 2009 February 9. Received 2009 February 9; in original form 2008 November 30

ABSTRACT

We study predictions for dark matter (DM) phase-space structure near the Sun based on high-resolution simulations of six galaxy haloes taken from the Aquarius project. The local DM density distribution is predicted to be remarkably smooth; the density at the Sun differs from the mean over a best-fitting ellipsoidal equidensity contour by less than 15 per cent at the 99.9 per cent confidence level. The local velocity distribution is also very smooth, but it differs systematically from a (multivariate) Gaussian distribution. This is not due to the presence of individual clumps or streams, but to broad features in the velocity modulus and energy distributions that are stable in both space and time and reflect the detailed assembly history of each halo. These features have a significant impact on the signals predicted for weakly interacting massive particle and axion searches. For example, weakly interacting massive particles recoil rates can deviate by ∼10 per cent from those expected from the best-fitting multivariate Gaussian models. The axion spectra in our simulations typically peak at lower frequencies than in the case of multivariate Gaussian velocity distributions. Also in this case, the spectra show significant imprints of the formation of the halo. This implies that once direct DM detection has become routine, features in the detector signal will allow us to study the DM assembly history of the Milky Way. A new field, 'DM astronomy', will then emerge.

Key words: methods: numerical – dark matter.

1 INTRODUCTION

In the 75 yr since Zwicky (1933) first pointed out the need for substantial amounts of unseen material in the Coma cluster, the case for a gravitationally dominant component of non-baryonic dark matter (DM) has become overwhelmingly strong. It seemed a long shot when Peebles (1982) first suggested that the DM might be an entirely new, weakly interacting, neutral particle with very low thermal velocities in the early universe, but such cold dark matter (CDM) is now generally regarded as the most plausible and consistent identification for the DM. Particle physics has suggested many possible CDM particles beyond the standard model. Two promising candidates are weakly interacting massive particles (WIMPs; see Lee & Weinberg 1977; Gunn et al. 1978; Ellis et al. 1984) and axions (Peccei & Quinn 1977b,a; Weinberg 1978; Wilczek 1978). Among the WIMPs, the lightest supersymmetric particle, the neutralino, is currently favoured as the most likely CDM particle, and the case will be enormously strengthened if the Large Hadron Collider (LHC) confirms supersymmetry. However, ultimate confirmation of the CDM paradigm can only come through the direct or indirect detection of the CDM particles themselves. Neutralinos, for example, are their own antiparticles and can annihilate to produce γ-rays and other particles. One goal of the recently launched Fermi γ-ray space telescope is to detect this radiation (Gehrels & Michelson 1999; Springel et al. 2008b).

Direct detection experiments, on the other hand, search for the interaction of CDM particles with laboratory apparatus. For WIMPs, detection is based on nuclear recoil events in massive, cryogenically cooled bolometers in underground laboratories (Jungman, Kamionkowski & Griest 1996); for axions, resonant microwave cavities in strong magnetic fields exploit the axion-photon conversion process (Sikivie 1985). Despite intensive searches, the only experiment which has so far reported a signal is DArk MAtter experiment (DAMA) (Bernabei et al. 2007) which has clear evidence for an annual modulation of their event rate of the kind expected from the Earth's motion around the Sun. The interpretation of this result is controversial, since it appears to require DM properties

⋆E-mail: vogelsma@mpa-garching.mpg.de

which are in conflict with upper limits established by other experiments (see Savage, Gondolo & Freese 2004; Gondolo & Gelmini 2005; Gelmini 2006, for a discussion and possible solutions). Regardless of this, recent improvements in detector technology may enable a detection of 'standard model' WIMPs or axions within a few years.

Event rates in all direct detection experiments are determined by the local DM phase-space distribution at the Earth's position. The relevant scales are those of the apparatus and so are extremely small from an astronomical point of view. As a result, interpreting null results as excluding specific regions of candidate parameter space must rely on (strong) assumptions about the fine-scale structure of phase space in the inner Galaxy. In most analyses, the DM has been assumed to be smoothly and spherically distributed about the Galactic Centre with an isotropic Maxwellian velocity distribution (e.g. Freese, Frieman & Gould 1988) or a multivariate Gaussian distribution (e.g. Green 2001; Ullio & Kamionkowski 2001; Helmi, White & Springel 2002). The theoretical justification for these assumptions is weak, and when numerical simulations of halo formation reached sufficiently high resolution, it became clear that the phase space of CDM haloes contains considerable substructure, both gravitationally bound subhaloes and unbound streams. As numerical resolution has improved, it has become possible to see structure closer and closer to the centre, and this has led some investigators to suggest that the CDM distribution near the Sun could, in fact, be almost fractal, with large density variations over short length-scales (e.g. Kamionkowski & Koushiappas 2008). This would have substantial consequences for the ability of direct detection experiments to constrain particle properties.

Until very recently, simulation studies were unable to resolve any substructure in regions as close to the Galactic Centre as the Sun (see Moore et al. 2001; Helmi, White & Springel 2002, 2003, e.g.). This prevented realistic evaluation of the likelihood that massive streams, clumps or holes in the DM distribution could affect event rates in Earth-bound detectors and so weaken the particle physics conclusions that can be drawn from null detections (see Savage, Freese & Gondolo 2006; Kamionkowski & Koushiappas 2008, for recent discussions). As we will show in this paper, a new age has dawned. As part of its Aquarius project (Springel et al. 2008a), the Virgo Consortium has carried out a suite of ultrahigh-resolution simulations of a series of Milky Way sized CDM haloes. Simulations of individual Milky Way haloes of similar scale have been carried out and analysed by Diemand et al. (2008), Zemp et al. (2009) and Stadel et al. (2008). Here, we use the Aquarius simulations to provide the first reliable characterizations of the local DM phase-space distribution and the detector signals which should be anticipated in WIMP and axion searches.

2 THE NUMERICAL SIMULATIONS

The cosmological parameters for the Aquarius simulation set are $\Omega_{\rm m} = 0.25$, $\Omega_\Lambda = 0.75$, $\sigma_8 = 0.9$, $n_{\rm S} = 1$ and $H_0 = 100\,h\,{\rm km\,s^{-1}}$ ${\rm Mpc^{-1}}$ with $h = 0.73$, where all quantities have their standard definitions. These parameters are consistent with current cosmological constraints within their uncertainties, in particular, with the parameters inferred from the *Wilkinson Microwave Anisotropy Probe* 1- and 5-yr data analyses (Spergel et al. 2003; Komatsu et al. 2009). Milky Way like haloes were selected for resimulation from a parent cosmological simulation which used 900^3 particles to follow the DM distribution in a $100\,h^{-1}$ Mpc periodic box. Selection was based primarily on halo mass ($\sim 10^{12}\,{\rm M}_\odot$) but also required that there should be no close and massive neighbour at $z = 0$. The Aquarius project resimulated six such haloes at a series of higher resolutions. The naming convention uses the tags Aq-A through Aq-F to refer to these six haloes. An additional suffix 1 to 5 denotes the resolution level. Aq-A-1 is the highest resolution calculation, with a particle mass of $1.712 \times 10^3\,{\rm M}_\odot$ and a virial mass of $1.839 \times 10^{12}\,{\rm M}_\odot$ it has more than a billion particles within the virial radius R_{200} which we define as the radius containing a mean density 200 times the critical value. The Plummer equivalent softening length of this run is 20.5 pc. Level-2 simulations are available for all six haloes with about 200 million particles within R_{200}. Further details of the haloes and their characteristics can be found in Springel et al. (2008a).

In the following analysis, we will often compare the six level-2 resolution haloes, Aq-A-2 to Aq-F-2. To facilitate this comparison, we scale the haloes in mass and radius by the constant required to give each a maximum circular velocity of $V_{\rm max} = 208.49\,{\rm km\,s^{-1}}$, the value for Aq-A-2.

3 SPATIAL DISTRIBUTIONS

The density of DM particles at the Earth determines the flux of DM particles passing through laboratory detectors. It is important, therefore, to determine not only the mean value of the DM density 8 kpc from the Galactic Centre, but also the fluctuations around this mean which may result from small-scale structure.

Throughout this section, we will refer to a coordinate system that is aligned with the principal axes of the inner halo, and which labels particles by an ellipsoidal radius $r_{\rm ell}$ defined as the semimajor axis length of the ellipsoidal equidensity surface on which the particle sits. We determine the orientation and shape of these ellipsoids as follows. For each halo, we begin by diagonalizing the moment of inertia tensor of the DM within the spherical shell $6\,{\rm kpc} < r < 12\,{\rm kpc}$ (after scaling to a common $V_{\rm max}$). This gives us a first estimate of the orientation and shape of the best-fitting ellipsoid. We then reselect particles with $6\,{\rm kpc} < r_{\rm ell} < 12\,{\rm kpc}$, recalculate the moment of inertia tensor and repeat until convergence. The resulting ellipsoids have minor-to-major axis ratios which vary from 0.39 for Aq-B-2 to 0.59 for Aq-D-2. The radius restriction reflects our desire to probe the DM distribution near the Sun. We note that we make use of $r_{\rm ell}$ only in this section. In the other parts of our paper, we will always use the standard spherical radius r.

We estimate the local DM distribution at each point in our simulations using a smoothed particle hydrodynamics (SPH) smoothing kernel adapted to the 64 nearest neighbours. We then fit a power law to the resulting distribution of $\ln \rho$ against $\ln r_{\rm ell}$ over the ellipsoidal radius range $6 < r_{\rm ell} < 12\,{\rm kpc}$. This defines a smooth model density field $\rho_{\rm model}(r_{\rm ell})$. We then construct a density probability distribution function (DPDF) as the histogram of $\rho/\rho_{\rm model}$ for all particles in $6 < r_{\rm ell} < 12\,{\rm kpc}$, where each is weighted by ρ^{-1} so that the resulting distribution refers to random points within our ellipsoidal shell rather than to random mass elements. We normalize the resulting DPDFs to have unit integral. They then provide a probability distribution for the local DM density at a random point in units of that predicted by the best-fitting smooth ellipsoidal model.

We have chosen an ellipsoidal radial range rather than a spherical one because we wish to characterize the variations in density caused by small-scale structure. We must therefore remove the strong angular dependence produced by the prolate structure of our haloes; the large minor-to-major axis ratios mentioned above lead to variations in density of up to an order of magnitude at fixed distance from halo centre. Since the stellar component of the Milky Way has a major effect on the shape of its dark halo at the solar circle, most likely causing it to be substantially rounder than our baryon-free

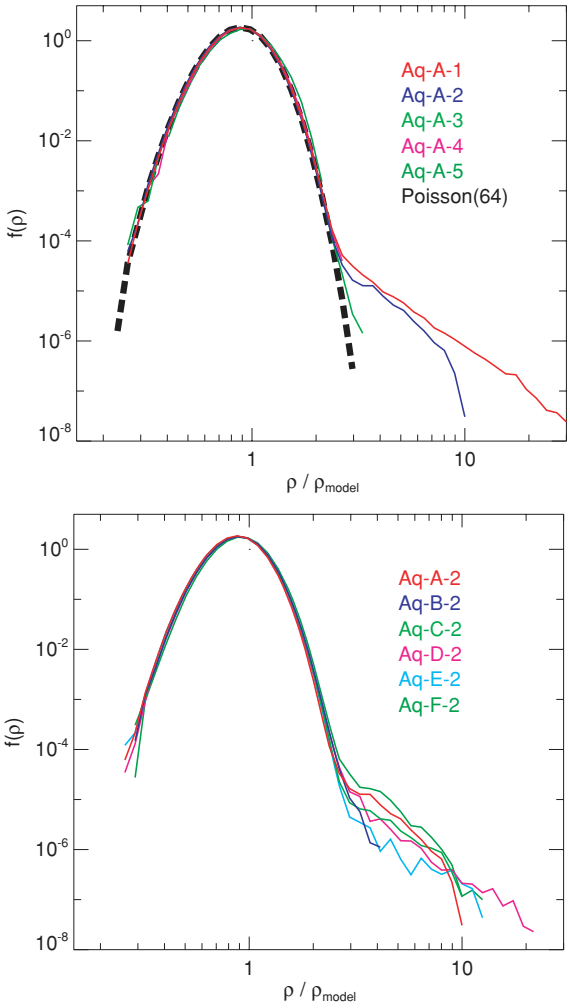

Figure 1. Top panel: DPDF for all resimulations of halo Aq-A measured within a thick ellipsoidal shell between equidensity surfaces with major axes of 6 and 12 kpc. The local DM density at the position of each particle, estimated using a SPH smoothing technique, is divided by the density of the best fit, ellipsoidally stratified, power-law model. The DPDF gives the distribution of the local density in units of that predicted by the smooth model at random points within the ellipsoidal shell. At these radii, only resolution levels 1 and 2 are sufficient to follow substructure. As a result, the characteristic power-law tail due to subhaloes is not visible at lower resolution. The fluctuation distribution of the smooth component is dominated by noise in our 64-particle SPH density estimates. The density distribution measured for a *uniform* (Poisson) particle distribution is indicated by the black dashed line. Bottom panel: as above, but for all level-2 haloes after rescaling to $V_{\rm max} = 208.49\,{\rm km\,s^{-1}}$. In all cases, the core of the DPDF is dominated by measurement noise and the fraction of points in the power-law tail due to subhaloes is very small. The chance that the Sun lies within a subhalo is $\sim 10^{-4}$. With high probability, the local density is close to the mean value averaged over the Sun's ellipsoidal shell.

haloes (e.g. Kazantzidis et al. 2004), only the small-scale structure of our simulations is directly relevant to DM detection experiments. The large-scale DM density distribution is more reliably inferred from dynamical modelling of Milky Way observations than from simulations of the kind we present here.

In Fig. 1, we show the DPDFs measured in this way for all resimulations of Aq-A (top panel) and for all level-2 haloes after scaling to a common $V_{\rm max}$ (bottom panel). Two distinct components are evident in both plots. One is smoothly and lognormally distributed around $\rho = \rho_{\rm model}$, the other is a power-law tail to high densities which contain less than 10^{-4} of all points. The power-law tail is not present in the lower resolution haloes (Aq-A-3, Aq-A-4 and Aq-A-5) because they are unable to resolve subhaloes in these inner regions. However, Aq-A-2 and Aq-A-1 give quite similar results, suggesting that resolution level 2 is sufficient to get a reasonable estimate of the overall level of the tail. A comparison of the six level-2 simulations then demonstrates that this tail has similar shape in different haloes, but a normalization which can vary by a factor of several. In none of our haloes does the fraction of the distribution in this tail rise above 5×10^{-5}. Furthermore, the arguments of Springel et al. (2008a) suggest that the total mass fraction in the inner halo (and thus also the total volume fraction) in subhaloes below the Aq-A-1 resolution limit is at most about equal to that above this limit. Hence, the chance that the Sun resides in a bound subhalo of any mass is of the order of 10^{-4}.

The striking similarity of the smooth lognormal component in all the distributions of Fig. 1 has nothing to do with actual density variations in the smooth DM distribution. It is, in fact, simply a reflection of the noise in our local density estimates. We demonstrate this by setting up a uniform Poisson point distribution within a periodic box and then using a SPH smoothing kernel adapted to the 64 nearest neighbours to associate a local density with each particle in exactly the same way as for our halo simulations. We can then construct a DPDF for these estimates (relative to their mean) in exactly the same way as before. The result is shown in the top panel of Fig. 1 as a dashed black line. It is an almost perfect fit to the smooth component in the simulations, and it would fit the other haloes equally well if plotted in the lower panel.

The fit is not perfect, however, and it is possible to disentangle the true scatter in density about the smooth model from the estimation noise. The latter is expected to be asymptotically lognormal for large neighbour numbers, and Fig. 1 shows that it is very close to lognormal for our chosen parameters. If we assume that the scatter in intrinsic density about the smooth model is also approximately lognormal, we can estimate its scatter as the square root of the difference between the variance of the simulation scatter and that of the noise: symbolically, $\sigma_{\rm intr} = \sqrt{\sigma^2_{\rm obs} - \sigma^2_{\rm noise}}$. Indeed, it turns out that the variance in $\ln(\rho/\rho_{\rm model})$ which we measure for our simulated haloes (excluding the power-law tail) is consistently higher than that which we find for our uniform Poisson distribution. Furthermore, tests show that the differences are stable if we change the number of neighbours used in the SPH estimator to 32 or 128, even though this changes the noise variance by factors of 2. This procedure gives the following estimates for rms intrinsic scatter around the smooth model density field in our six level-2 haloes, Aq-A-2 to Aq-F-2: 2.2, 4.4, 3.7, 2.1, 4.9 and 4.0 per cent, respectively. The very large particle number in the radial range we analyse results in a standard error on these numbers which is well below 0.01 for all haloes. Thus, we can say with better than 99.9 per cent confidence that the DM density at the Sun's position differs by less than 15 per cent from the average over the ellipsoidal shell on which the Sun sits. This small scatter implies that the density field in the inner halo is remarkably well described by a smooth, ellipsoidal, power-law model. This qualitative behaviour was predicted analytically by Kamionkowski & Koushiappas (2008), although the fluctuation level we find for the smooth component is much smaller than they suggested.

We conclude that the local density distribution of DM should be very smooth. Bound clumps are very unlikely to have any effect on direct detection experiments. The main reason for this is

the short dynamical time at the solar radius (about 1 per cent of the Hubble time). This results in very efficient mixing of unbound material and the stripping of all initially bound objects to a small fraction of the maximum mass they may have had in the past (see Vogelsberger et al. 2008, for a discussion of these processes). Note that the actual density of DM in the solar neighbourhood and the shape of the equidensity surfaces of the Milky Way's DM distribution will depend on how the gravitational effects of the baryonic components have modified structure during the system's formation. Unfortunately, the shape of the inner DM halo of the Milky Way is poorly constrained observationally (Helmi 2004; Law, Johnston & Majewski 2005). The dissipative contraction of the visible components probably increased the density of the DM component and made it more axisymmetric (e.g. Gnedin et al. 2004; Kazantzidis et al. 2004) but these processes are unlikely to affect the level of small-scale structure. The very smooth behaviour we find in our pure DM haloes should apply also to the more complex real Milky Way.

4 VELOCITY DISTRIBUTIONS

The velocity distribution of DM particles near the Sun is also an important factor influencing the signal expected in direct detection experiments. As mentioned in the Introduction, most previous work has assumed this distribution to be smooth, and either Maxwellian or multivariate Gaussian. Very different distributions are possible in principle. For example, if the local density distribution is a superposition of a relatively small number of DM streams, the local velocity distribution would be effectively discrete with all particles in a given stream sharing the same velocity (Sikivie, Tkachev & Wang 1995; Stiff, Widrow & Frieman 2001; Stiff & Widrow 2003). Clearly, it is important to understand whether such a distribution is indeed expected, and whether a significant fraction of the local mass density could be part of any individual stream.

We address this issue by dividing the inner regions of each of our haloes into cubic boxes 2 kpc on a side, and focusing on those boxes centred between $7 < r < 9$ kpc from halo centre. In Aq-A-1, each 2 kpc box contains 10^4 to 10^5 particles, while in the level-2 haloes they contain an order of magnitude fewer. For every box, we calculate a velocity dispersion tensor and study the distribution of the velocity components along its principal axes. In almost all boxes, these axes are closely aligned with those the ellipsoidal equidensity contours discussed in the last section. We also study the distribution of the modulus of the velocity vector within each box. The upper four panels of Fig. 2 show these distributions of a typical 2 kpc box at the solar circle in Aq-A-1 (solid red lines). Here, and in the following plots, we normalize distributions to have unit integral. The black dashed lines in each panel show a multivariate Gaussian distribution with the same mean and dispersion along each of the principal axes. The difference between the two distributions in each panel is plotted separately just above it. This particular box is quite typical, in that we almost always find the velocity distribution to be significantly anisotropic, with a major axis velocity distribution which is platykurtic, and distributions of the other two components which are leptokurtic. Thus, the velocity distribution differs significantly from Maxwellian, or even from a multivariate Gaussian. The individual velocity components have very smooth distributions with no sign of spikes due to individual streams. This also is a feature which is common to almost all our 2 kpc boxes. It is thus surprising that the distribution of the velocity modulus shows clear features in the form of bumps and dips with amplitudes of several tens of per cent.

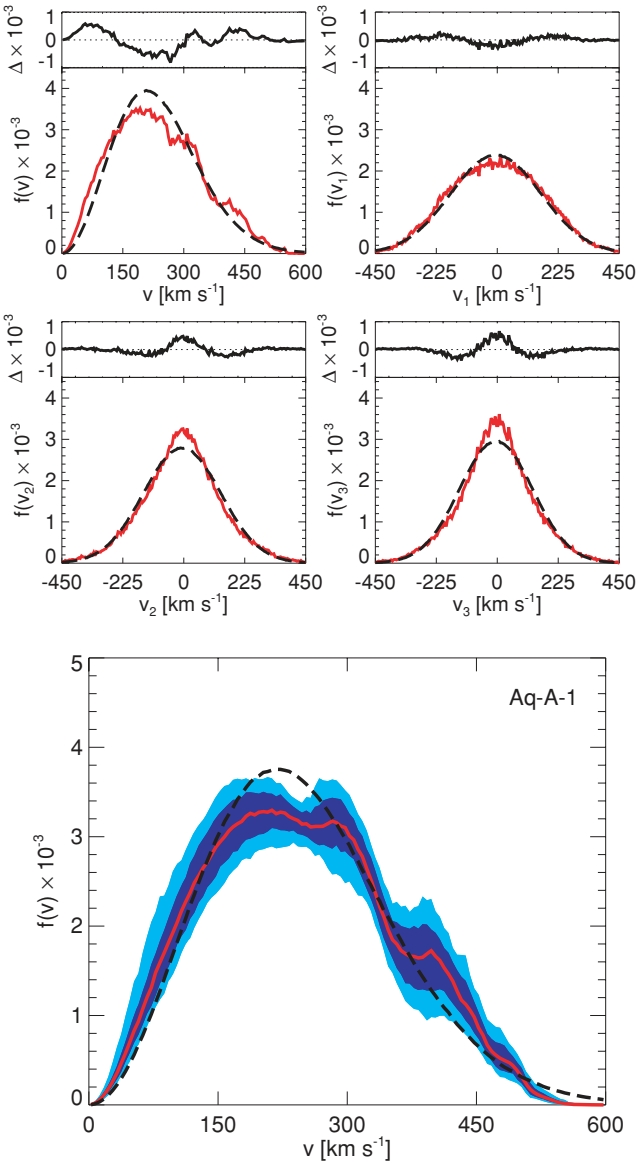

Figure 2. Top four panels: velocity distributions in a 2 kpc box at the solar circle for halo Aq-A-1. v_1, v_2 and v_3 are the velocity components parallel to the major, intermediate and minor axes of the velocity ellipsoid; v is the modulus of the velocity vector. Red lines show the histograms measured directly from the simulation, while black dashed lines show a multivariate Gaussian model fit to the individual component distributions. Residuals from this model are shown in the upper part of each panel. The major axis velocity distribution is clearly platykurtic, whereas the other two distributions are leptokurtic. All three are very smooth, showing no evidence for spikes due to individual streams. In contrast, the distribution of the velocity modulus, shown in the upper left-hand panel, shows broad bumps and dips with amplitudes of up to 10 per cent of the distribution maximum. Lower panel: velocity modulus distributions for all 2 kpc boxes centred between 7 and 9 kpc from the centre of Aq-A-1. At each velocity, a thick red line gives the median of all the measured distributions, while a dashed black line gives the median of all the fitted multivariate Gaussians. The dark and light blue contours enclose 68 and 95 per cent of all the measured distributions at each velocity. The bumps seen in the distribution for a single box are clearly present with similar amplitude in all boxes, and so also in the median curve. The bin size is 5 km s^{-1} in all plots.

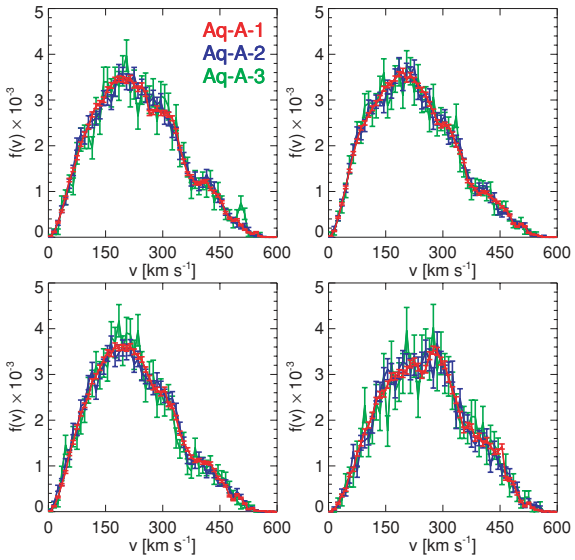

Figure 3. Distributions of the velocity modulus in four well separated 2 kpc boxes about 8 kpc from the centre of Aq-A. Results are shown for each region from each of the three highest resolution simulations. Error bars are based on Poisson statistics. The different resolutions agree within their error bars, and show the same bumps in all four boxes. For the purpose of this plot, we have chosen a larger bin for our histograms, 10 km s^{-1} as compared to 5 km s^{-1} in our other velocity plots. For this bin size, the statistical noise in Aq-A-1 is barely visible.

To see how these features vary with position, we overlaid the distributions of the velocity modulus for all 2 kpc boxes centred between 7 and 9 kpc from the centre of Aq-A-1 (bottom panel of Fig. 2). We superpose both the directly measured distributions and the predictions from the best-fitting multivariate Gaussians. At each velocity, the solid red line shows the median value of all the directly measured distributions, while the dashed black line is the median of all the multivariate Gaussian fits. The dark and light regions enclose 68 and 95 per cent of all the individual measured distributions at each velocity.

It is interesting to note that the bumps in the velocity distribution occur at approximately the same velocity in all boxes. This suggests that they do not reflect local structures, but rather some global property of the inner halo. In Fig. 3, we show velocity modulus distribution for four different boxes in Aq-A at the three highest resolutions (levels 1, 2 and 3). The error bars are based on Poisson statistics in each velocity bin. Clearly, the same bumps are present in all boxes and at all resolutions. Thus, they are a consequence of real dynamical structure that converges with increasing numerical resolution.

In Fig. 4, we make similar plots of the velocity modulus distribution for all level-2 haloes. These distributions are quite smooth. The sharp peak in Aq-B-2 is due to a single 2 kpc box where 60 per cent of the mass is contained in a single subhalo. No other box in this or any other halo has more than 1.5 per cent of its mass in a single subhalo. The great majority of boxes contain no resolved subhalo at all. Although the details of the median distributions vary between haloes, they share some common features. The low-velocity region is more strongly populated in all cases than predicted by the multivariate Gaussian model. In all cases, the peak of the distribution is depressed relative to the multivariate Gaussian. At moderately high velocities, there is typically an excess. Finally, and perhaps most importantly, all the distributions show bumps and dips of the kind discussed above. These features appear in different places in different haloes, but they appear at similar places for all boxes in a given halo. The left-hand panel of Fig. 5 superposes the median velocity modulus distributions of all level-2 haloes and plots their mean as a black dashed line. The middle panel shows the deviations of the individual haloes from this mean. The amplitudes of the deviations are similar in different haloes and at low and high velocities. In percentage terms, the deviations are largest at high velocity reaching values of 50 per cent or more, as can be seen from the right-hand panel of Fig. 5.

The bumps in the velocity distribution are too broad to be explained by single streams. Furthermore, single streams are not massive enough to account for these features. This is shown more clearly in Fig. 6 where we illustrate some streams in velocity space for a 2 kpc box in halo Aq-A-1. Different colours here indicate particles that belonged to different FoF groups at redshift 4.2. For clarity, we only show streams from groups that contribute at least 10 particles to this volume (0.025 per cent of the total number of particles present at this location). There are 27 such objects. If we consider all FoF groups that contribute more than two particles to the volume shown in Fig. 6, we find that a given FoF group contributes streams that are typically only populated by two particles (0.005 per cent of the total mass in the box). This implies that most of the groups contribute several streams of very low density. The most prominent streams have ∼40 particles, i.e. ∼0.1 per cent of the mass in this volume. This clearly shows that streams are expected to be neither dense nor massive in the solar vicinity.

The most prominent streams typically occupy the tail of the velocity distribution in these local boxes. The excess of particles moving with similar velocities and high kinetic energies can be measured using a velocity correlation function, as shown by Helmi et al. (2002).

5 ENERGY DISTRIBUTIONS

We have seen that the distributions of individual velocity components in localized regions of space are very smooth, whereas the velocity modulus distribution shows clear bumps. Taken together with the fact that these bumps occur at similar velocities in regions on opposite sides of the halo centre, this indicates that we must be seeing features in the energy distribution of DM particles.

To investigate this further, we estimate the mean phase-space density $\bar{f}$ as a function of energy in each of our haloes using the properties of the particles at radii r between 6 and 12 kpc. Clearly, our haloes are not perfectly in equilibrium and far from spherical. Thus, their phase-space densities will only approximately be describable as functions of the integrals of motion, and they will depend significantly on integrals other than the energy. Nevertheless, we can estimate a mean phase-space density as a function of energy by taking the total mass of particles with $6 < r < 12$ kpc and energies in some small interval and dividing it by the total phase-space volume corresponding to this radius and energy range, e.g.

$$\bar{f}(E) \equiv \frac{\mathrm{d}M}{\mathrm{d}E}\frac{1}{g(E)}, \tag{1}$$

where $\bar{f}(E)$ is the energy-dependent mean phase-space density and

$$g(E)\,\mathrm{d}E \equiv 4\pi \int_{\mathcal{V}, E>\Phi(\boldsymbol{x})} \mathrm{d}^3\boldsymbol{x}\ \sqrt{2\left[E-\Phi(\boldsymbol{x})\right]}\ \mathrm{d}E, \tag{2}$$

is the phase-space volume with orbital energy in the range $(E, E + \mathrm{d}E)$ and halocentric radius in the range $6 < r < 12$ kpc. We note that

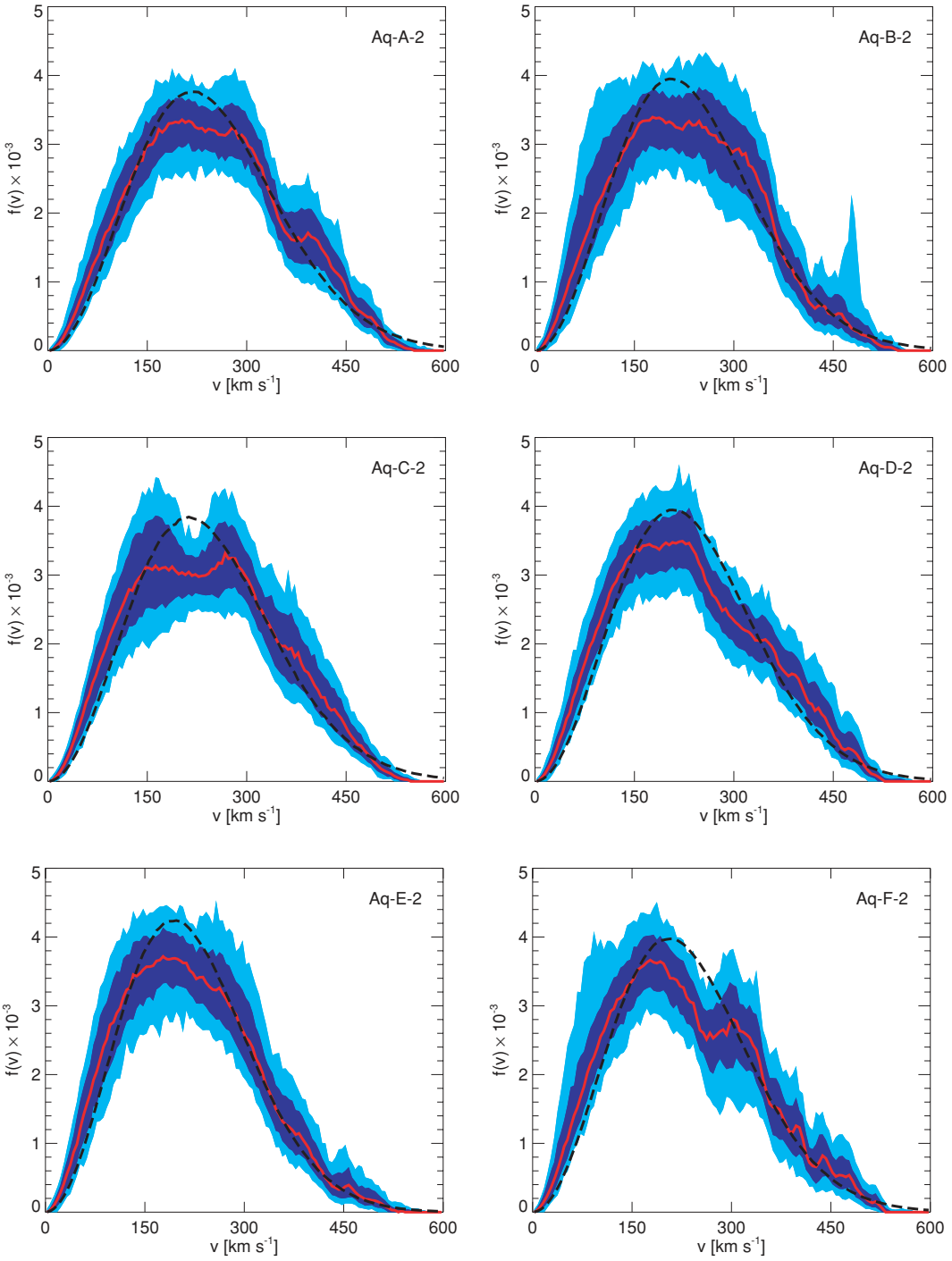

Figure 4. Velocity modulus distributions in exactly the same format as the bottom panel of Fig. 2 but for all six of our haloes at level-2 resolution. All distributions are smooth. Only in Aq-B-2 do we see a strong spike which is due to a single box which has 60 per cent of its mass (though a small fraction of its volume) in a single subhalo. No other box in any of the distributions has a subhalo contributing more than 1.5 per cent of the mass. All distributions show characteristic broad bumps which are present in all boxes in a given halo, and so in its median distribution. These bumps are in different places in different haloes.

our definition of $\bar{f}(E)$ returns the true $f(E)$ for any averaging volume in any system in which the phase-space distribution function only depends on energy.

The differential energy distribution is easily calculated by binning the energies of all particles between 6 and 12 kpc. The phase-space volume can be calculated by solving for the gravitational potential at the position of all simulation particles and then using these as a Monte Carlo sampling of configuration space in the relevant integrals. Taking the ratio then yields the desired estimate of $\bar{f}(E)$. We note that both the mass M and the differential phase-space volume per unit energy $g(E)$ depend strongly on the geometric region over which they are evaluated, in the present case, a thick spherical shell between 6 and 12 kpc. We find, however, that the mean phase-space density defined by equation (1) depends only very

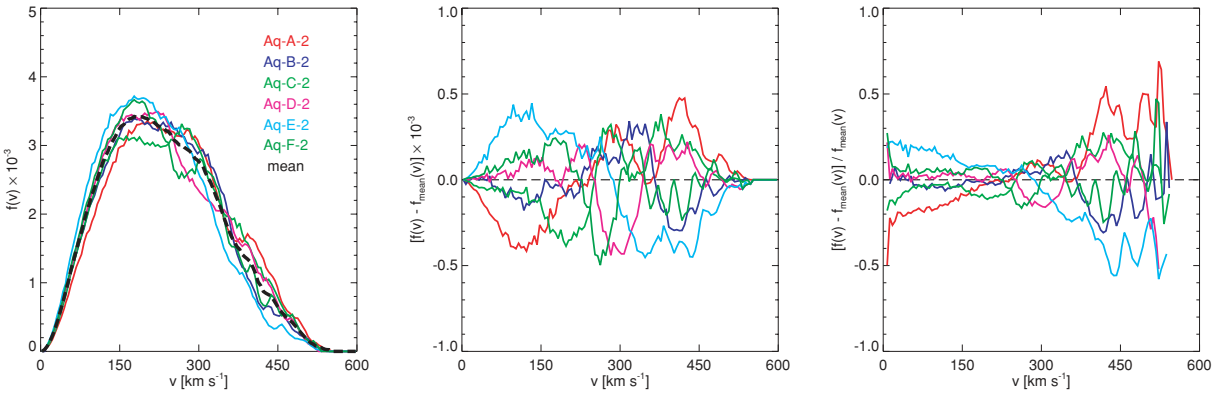

Figure 5. Left-hand panel: median velocity modulus distributions for all six level-2 haloes repeated from Fig. 4. The black dashed line is the mean of these distributions. Middle panel: deviations of the velocity modulus distribution of each of the six haloes from the sample mean. The amplitude of the various bumps is similar in different haloes and over the whole velocity range. It reaches more than 10 per cent of the amplitude of the mean distribution. Right-hand panel: relative deviations of the individual velocity modulus distributions from their sample mean. Typical relative deviations are about 30 per cent, but they can exceed 50 per cent at higher velocities.

weakly on the region chosen, for example on the radii of our spherical shell. Indeed, as can be inferred from Fig. 2, it is very similar to that obtained for any 2 kpc cube at $R = 8$ kpc. Thus, in practise, the weighting implied by the average over the other integrals of motion which is implicit in equation (1) does not depend much on the geometry of the region chosen.

In Fig. 7, we show $\bar{f}(E)$ measured in this way for all our simulations of Aq-A. We express the energy in units of $v_{\rm max}^2$ and we take the zero-point of the gravitational potential to be its average value on a sphere of radius 8 kpc. As a result, the measured energy distribution extends to slightly negative values. Note how well the distribution converges at the more strongly bound energies. At higher energies, the convergence between the level-1 and -2 resolutions is still very good. This demonstrates that we can robustly measure the mean phase-space density distribution. Furthermore, we see clear wiggles that reproduce quite precisely between the different resolutions.

Fig. 8 shows similarly estimated mean phase-space density distributions for Aq-A-2 at five different times separated by about 300 Myr. This is longer than typical orbital periods in the region we are studying. Despite this, the wiggles at energies below $2.4v_{\rm max}^2$ are present over the complete redshift range shown. This demonstrates that these features are well mixed, and the mean phase-space density distribution has reached a coarse-grained equilibrium. In contrast, the variability of the wiggles in the part of the distribution corresponding to weakly bound particles (where the orbital periods are much larger) shows that these must be due to individual streams or to superpositions of small numbers of streams, which have not yet phase-mixed away.

To estimate what these mean phase-space density distributions should look like for a 'smooth' system, we average the functions found in our six individual level-2 haloes. In Fig. 9, we superpose these six functions and their mean $\langle\bar{f}\rangle$ (the black dashed line). The similarity of the different distribution functions at high-binding energies suggests a near-universal shape for $\bar{f}(E)$. At lower binding energies, individual haloes deviate quite strongly from $\langle\bar{f}\rangle$. This can be seen more clearly in Fig. 10 where we plot $\log(\bar{f}/\langle\bar{f}\rangle)$, the decimal logarithm of the ratio of the mean phase-space density of an individual halo to the average. The lower axis is orbital energy in units of $v_{\rm max}^2$, while the upper axis is the corresponding DM particle velocity at the solar circle. In this plot, one can clearly see the wiggles, which are located at different energies for different haloes. For $v_{8\,\rm kpc} < 350\,{\rm km\,s^{-1}}$, the mean phase-space densities for all haloes satisfy $0.7 < \bar{f}/\langle\bar{f}\rangle < 1.4$. For low-binding energies (velocities of 600 km s^{-1} or more at the solar circle), this ratio can exceed by a factor of 10.

These features in the mean phase-space density distribution must be related to events in the formation of each halo. To demonstrate this explicitly, we have computed $\bar{f}(E)$ separately for particles which were accreted on to two of our haloes (i.e. first entered the main progenitor FoF group) at different epochs. The upper left-hand panel of Fig. 11 shows that Aq-A-2 had a very 'quiet' merger history. Material accreted at different times is arranged in a very orderly way in energy space. All the most strongly bound particles were accreted before redshift 5, and material accreted at successively later times forms a series of 'shells' in energy space. The most weakly bound wiggles are due entirely to the most recently accreted material, and progressively more bound bumps can be identified with material accreted at earlier and earlier times. In contrast, the top right-hand panel shows that Aq-F-2 had a very 'active' merger history, with a major merger between $z = 0.75$ and 0.68. The correspondence between binding energy and epoch of accretion is much less regular than for Aq-A-2, and much of the most bound material actually comes from the object which fell in between $z = 0.75$ and 0.68. It is also striking that many of the wiggles in this object are present in material that accreted at quite different times, suggesting that they may be non-steady coherent oscillations rather than stable structures in energy space. Nevertheless, in both haloes one can identify features in the mean phase-space density distribution with particles accreted at certain epochs, and in both haloes the most weakly bound particles were added only very recently. Note that the mean phase-space density of this material is very low, so it contributes negligibly to the overall local DM density. In the bottom panels of Fig. 11, we show the $\bar{f}(E)$ distributions of particles which were associated with a single, massive FoF group which was identified at $z = 6.85$ in the case of Aq-A-2 and at $z = 0.75$ in the case of Aq-F-2. The wiggles in the strongly bound part of Aq-A-2 are clearly due to this early merger event, while the later merger in Aq-F-2 is responsible for most of the material accreted in $0.56 < z < 0.81$ and for most of the strong features in the mean phase-space density distribution.

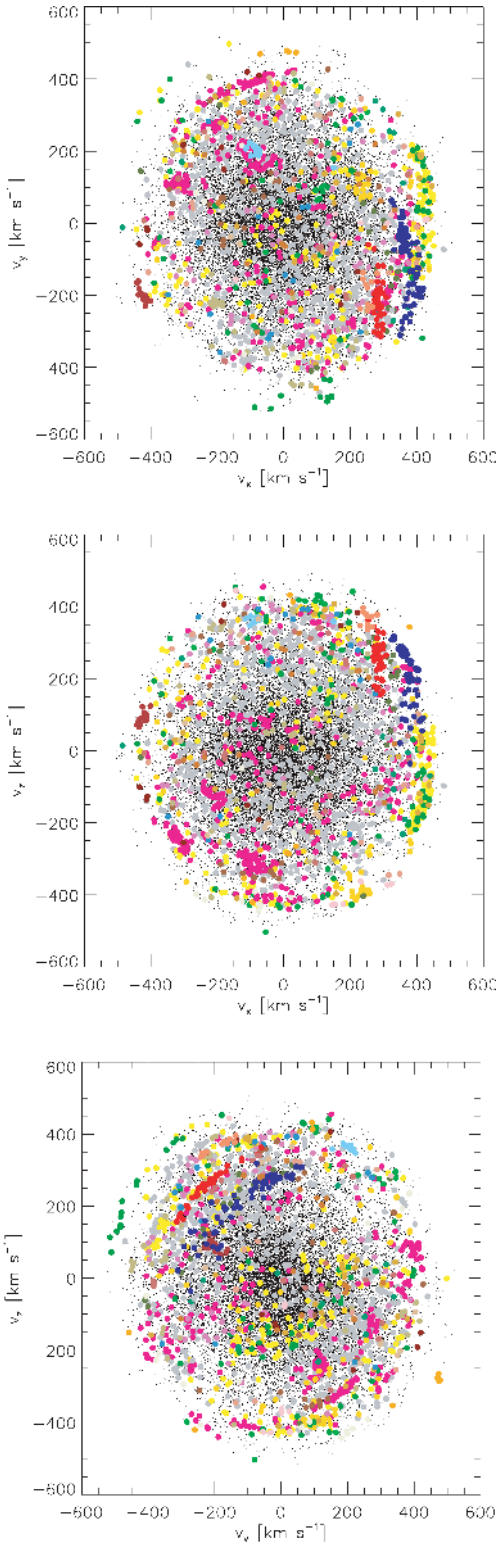

Figure 6. Streams in velocity space for a 2 kpc box ∼8 kpc from the centre of Aq-A-1. Different colours stand for particles associated with different FoF groups at redshift 4.2. Only groups contributing more than 10 particles are shown. The box contains 27 such objects and has in total 41 143 particles (shown as small black points) of which 1796 come from these groups. Clearly, particles originating from the same group cluster in velocity space and build streams; often many streams per group.

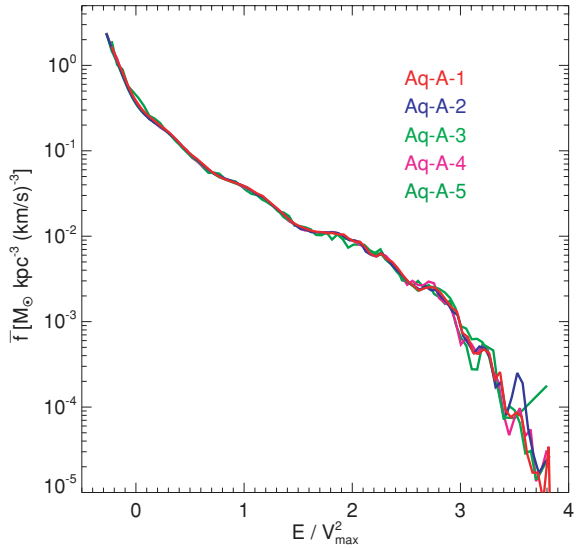

Figure 7. Mean phase-space density distribution as a function of energy for Aq-A for particles in a spherical shell between 6 and 12 kpc and for all five resolution levels. Especially at high-binding energies, the convergence is very good. Features in the distribution function are visible at all resolutions for energies below 2.7 $v^2_{\rm max}$, despite the fact that the mass resolution differs by more than a factor of 1800 between Aq-A-1 and Aq-A-5. The less bound parts show more variation from resolution to resolution but still agree well between Aq-A-1 and Aq-A-2.

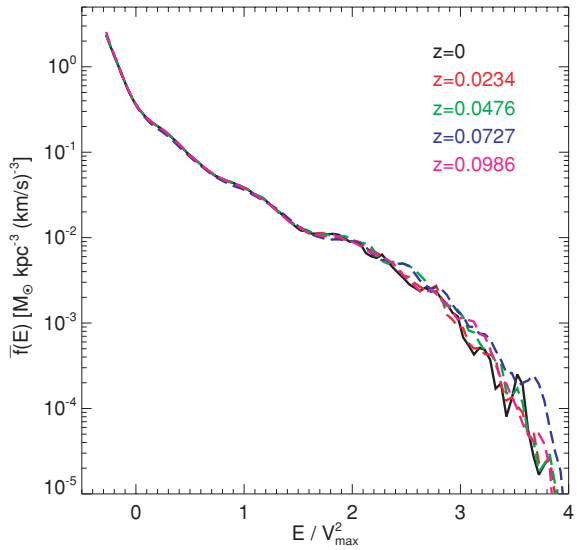

Figure 8. Evolution of the mean phase-space density distribution of Aq-A-2 over four time intervals of about 300 Myr. Below 2.4 $v^2_{\rm max}$, the mean phase-space density distribution is time-independent, implying that the system has reached coarse-grained equilibrium. The small bumps at these energies are therefore well-mixed features in action space. The variability of the features in the weakly bound part of the distribution shows that they are due to individual streams and therefore change on the time-scale of an orbital period. Note that the mean phase-space density at these energies is almost three orders of magnitude below that of the most bound particles.

We conclude that these features in the energy distribution should open the window to 'DM astronomy' once experiments reach the sensitivity needed for routine detection of DM particles. We will then be able to explore the formation history of the Milky Way using the DM energy distribution.

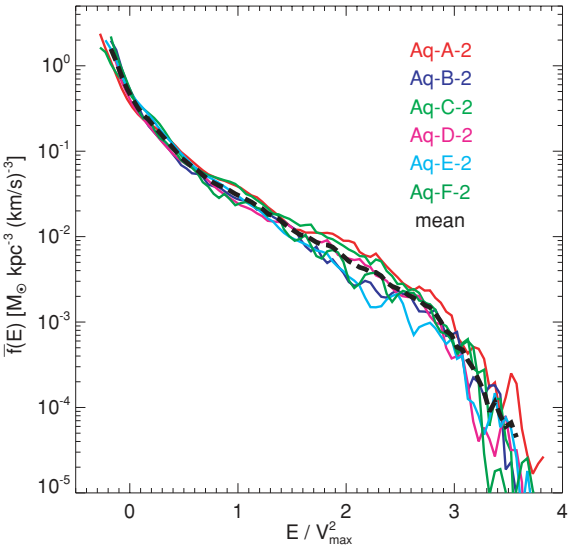

Figure 9. Scaled mean phase-space density distribution for all level-2 haloes. In addition to scaling according to v_{max}, we have also corrected for a zero-point offset in the potential energy between different haloes. The black dashed line shows the average mean phase-space density distribution for our halo sample. At high-binding energies, the scatter between average and individual halo mean phase-space density distributions is quite small, showing that this part of the distribution is near-universal. At low-binding energies, large amplitude features are visible in all haloes. These features differ from halo to halo and are related to recent events in their formation histories.

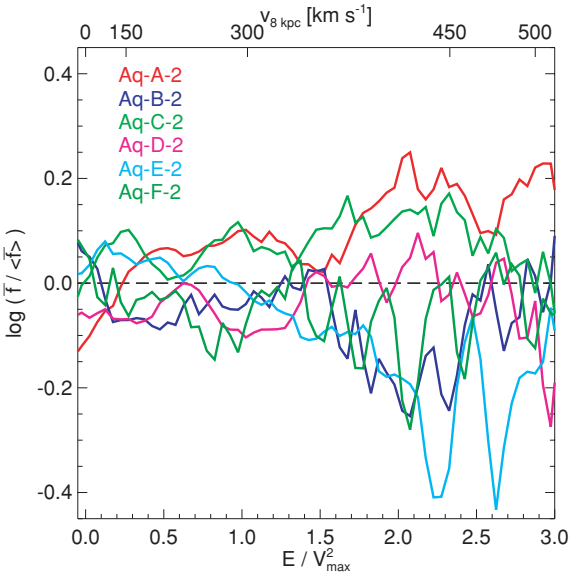

Figure 10. Deviations of the individual mean phase-space density distributions from the average over our sample of level-2 haloes. We focus here on the more bound part. The lower x-axis shows the orbital energy while the upper one shows the corresponding velocity 8 kpc distance from halo centre. The amplitude of features increases for $v_{8\,kpc} > 350\,km\,s^{-1}$. At even lower binding energies, $E > 3\ v_{max}$ deviations can reach an order of magnitude, see Fig. 9.

6 DETECTOR SIGNALS

We will now use the spatial and velocity distributions explored above to calculate expected detector signals. The main question here is how the non-Gaussian features of the velocity distribution influence these signals. Our results show that features due to sub-haloes or massive streams are expected to be unimportant. On the other hand, deviations of the velocity distributions from a perfect Gaussians in terms of general shape, bumps and dips can have an impact on detector signals.

There are currently more than 20 direct detection experiments searching for Galactic DM, most of them focusing on WIMPs. For these, the detection scheme is based on nuclear recoil with the detector material. The differential WIMP elastic scattering rate can be written as (Jungman et al. 1996)

$$R = \mathcal{R}\,\rho_0\,T(E,t), \tag{3}$$

where $\mathcal{R}$ encapsulates the particle physics parameters (mass and cross-section of the WIMP; form factor and mass of target nucleus), ρ_0 is the local DM density that we assume to be constant based on the results of Section 3 and

$$T(E,t) = \int_{v_{min}}^{\infty} \mathrm{d}v\ \frac{f_v(t)}{v}, \tag{4}$$

where f_v is the WIMP speed distribution in the rest frame of the detector integrated over the angular distribution. v_{min} here is the detector-dependent minimum WIMP speed that can cause a recoil of energy E:

$$v_{min} = \left(\frac{E(m_\chi + m_a)^2}{2m_\chi^2 m_a}\right)^{1/2}, \tag{5}$$

where m_χ is the WIMP mass and m_a is the atomic mass of the target nucleus. To get detector-independent results, we set $\mathcal{R} = 1$ in the following. [1]

The recoil rate shows a annual modulation over the year (Drukier, Freese & Spergel 1986). To take this into account, we add the Earth's motion to the local box velocities to transform Galactic rest-frame velocities into the detector frame. We model the motion of the Earth according to Lewin & Smith (1996) and Binney & Merrifield (1998). Let $\boldsymbol{v}_E = \boldsymbol{u}_r + \boldsymbol{u}_S + \boldsymbol{u}_E$ be the velocity of the Earth relative to the Galactic rest frame decomposed into Galactic rotation $\boldsymbol{u}_r$, the Sun's peculiar motion $\boldsymbol{u}_S$ and the Earth's velocity relative to the Sun $\boldsymbol{u}_E$. In Galactic coordinates, these velocities can be written as

$$\begin{aligned} \boldsymbol{u}_r &= (0, 222.2, 0)\ \mathrm{km\ s^{-1}}, \\ \boldsymbol{u}_S &= (10.0, 5.2, 7.2)\ \mathrm{km\ s^{-1}}, \\ e_{E,i} &= u_E(\lambda)\cos(\beta_i)\sin(\lambda - \lambda_i), \\ u_E(\lambda) &= \langle u_E\rangle[1 - e\sin(\lambda - \lambda_i)] \end{aligned} \tag{6}$$

where $i = R, \phi, z$, λ is the ecliptic longitude ($\lambda_0 = (13 \pm 1)^\circ$), $\langle u_E\rangle = 29.79\,km\,s^{-1}$ is the mean velocity of the Earth around the Sun and the ellipticity of the Earth orbit is $e = 0.016\,722$. The $\boldsymbol{u}_r$ value is based on a combination of a large number of independent determinations of the circular velocity by Kerr & Lynden-Bell (1986). We note that this value has a standard deviation of 20 km s^{-1}. For the constant β and λ angles, we take

$$\begin{aligned} (\beta_r, \beta_\phi, \beta_z) &= (-5.^\circ5303,\ 59.^\circ575,\ 29.^\circ812) \\ (\lambda_r, \lambda_\phi, \lambda_z) &= (266.^\circ141,\ -13.^\circ3485,\ 179.^\circ3212). \end{aligned} \tag{7}$$

[1] This also implies that we assume the form factor to be constant. Any other form factor will change the shape of the recoil spectrum. Since we are not interested in the exact shape of the spectrum, but in deviations expected due to different velocity distributions, we neglect form factor effects in the following.

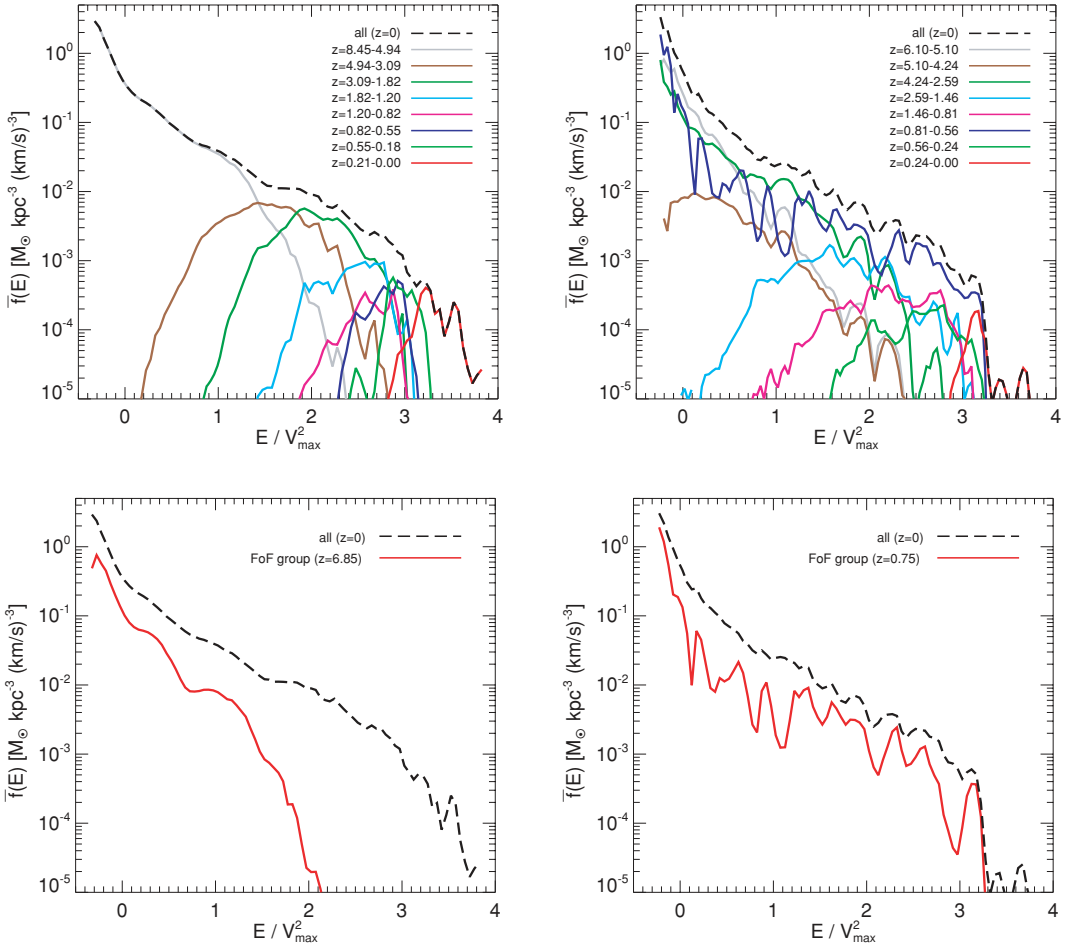

Figure 11. Top row: contributions to the present-day mean phase-space density distribution from particles accreted at different epochs (indicated by different colours). The top left-hand panel shows the build-up of the mean phase-space density distribution for halo Aq-A-2. This halo has a quiescent formation history with no recent mergers. The top right-hand panel is a similar plot for Aq-F-2, which underwent a major merger between $z = 0.75$ and 0.68. Bottom row: these plots isolate the contribution of a single, massive FoF group to the $z = 0$ mean phase-space density distributions. For Aq-A-2, this group was identified at $z = 6.85$ and for Aq-F-2 at $z = 0.75$. In both cases, it is clear that material from the group is responsible for some of the features seen in the present-day mean phase-space density distribution.

The ecliptic longitude can be written as

$$\begin{aligned}\lambda(t) &= L(t) + 1.^{\circ}915 \sin g(t) + 0.^{\circ}020 \sin 2g(t),\\ L(t) &= 280.^{\circ}460 + 0.^{\circ}985\,6474t,\\ g(t) &= 357.^{\circ}528 + 0.^{\circ}985\,6003t,\end{aligned} \tag{8}$$

where t is the fractional day number relative to noon (UT) on 1999 December 31 (J2000.0). We refer to a day number relative to 2008 December 31 in our plots. In what follows we will assume that the R-direction is always aligned with the major axis of the principal axis frame of the velocity ellipsoid in each box and the ϕ- and z-directions, with the intermediate and short axes. This is needed to add the Earth's motion to the box velocities, and to transform the velocity vectors in each box to the detector frame.

Clearly, the deviations of the velocity distribution from a perfect multivariate Gaussian found in the previous sections will also alter the recoil spectrum, because the velocity integral $T(E, t)$ effectively measures the $1/v$-weighted area under the velocity curve. As in the previous sections, we compare the results obtained directly from the simulations to the expectation for a best-fitting multivariate Gaussian distribution. In Fig. 12, we plot recoil spectra ratios for the three highest resolution simulations of Aq-A (left-hand panel) and the level-2 (right-hand panel) simulations of the other haloes. For these plots, we averaged the recoil rate over a year for individual boxes. The rates are calculated using the simulation velocity distribution ($\langle R \rangle$) and the best-fitting Gaussian model for each box ($\langle R_{\rm gauss} \rangle$). The plots show the median of the ratios $\langle R \rangle / \langle R_{\rm gauss} \rangle$ over all boxes. Since we assume that the density ρ_0 is constant in a given box, it drops out when calculating the ratios. The x-axis measures the energy in dimensionless $\beta = v/c$ values. For a given detector, this can easily be converted to keV, assuming the masses m_χ and $m_{\rm a}$ are given in GeV/c^2:

$$E = \frac{2m_\chi^2 m_{\rm a}}{(m_\chi + m_{\rm a})^2} c^2 \beta^2 \times 10^6\,{\rm keV}. \tag{9}$$

Fig. 12 clearly shows that in all level-2 haloes the expected recoil spectrum based on a multivariate Gaussian model can differ by up to 10 per cent from the directly predicted simulation result. Furthermore, the behaviour of the deviations seems to be similar in all cases, especially at low energies, where we already found that the mean phase-space density distribution is nearly universal. The similarity in the deviations between the different haloes is due to the fact that the velocity distributions all differ in a

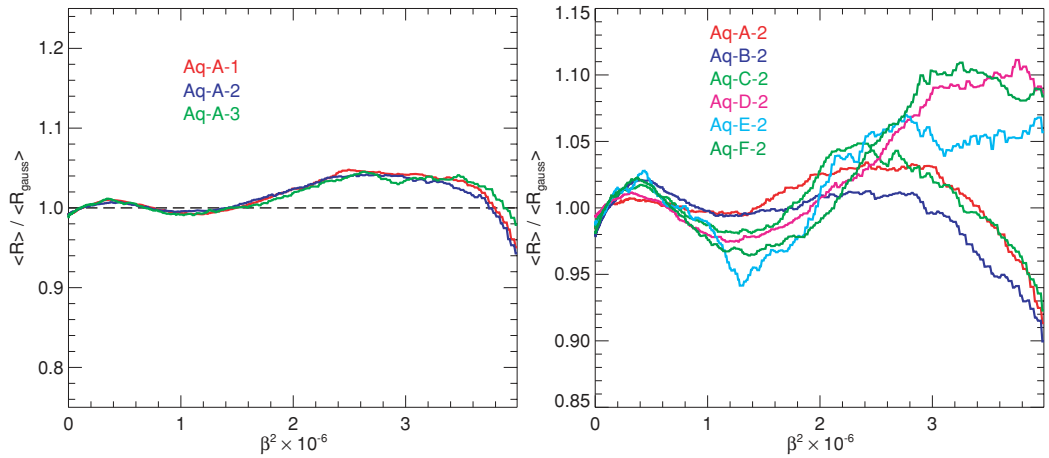

Figure 12. Recoil spectra ratio for the three highest resolution simulations of Aq-A (left-hand panel) and the level-2 (right-hand panel) simulations of the other haloes. For these plots, we averaged the recoil rate over a year for every box and then calculated the median recoil rate ratio $\langle R\rangle/\langle R_{\rm gauss}\rangle$ of the rates for the simulation and the best-fitting multivariate Gaussian distribution. The x-axis is directly proportional to the energy. In all level-2 haloes, the expected recoil spectrum based on a multivariate Gaussian can be wrong by about 10 per cent depending on the energy. Furthermore, the behaviour of the deviations seems quite similar. This is due to the fact that the velocity distributions differ in a characteristic way from a multivariate Gaussian. The deviations in the recoil spectra are typically highest at high energies.

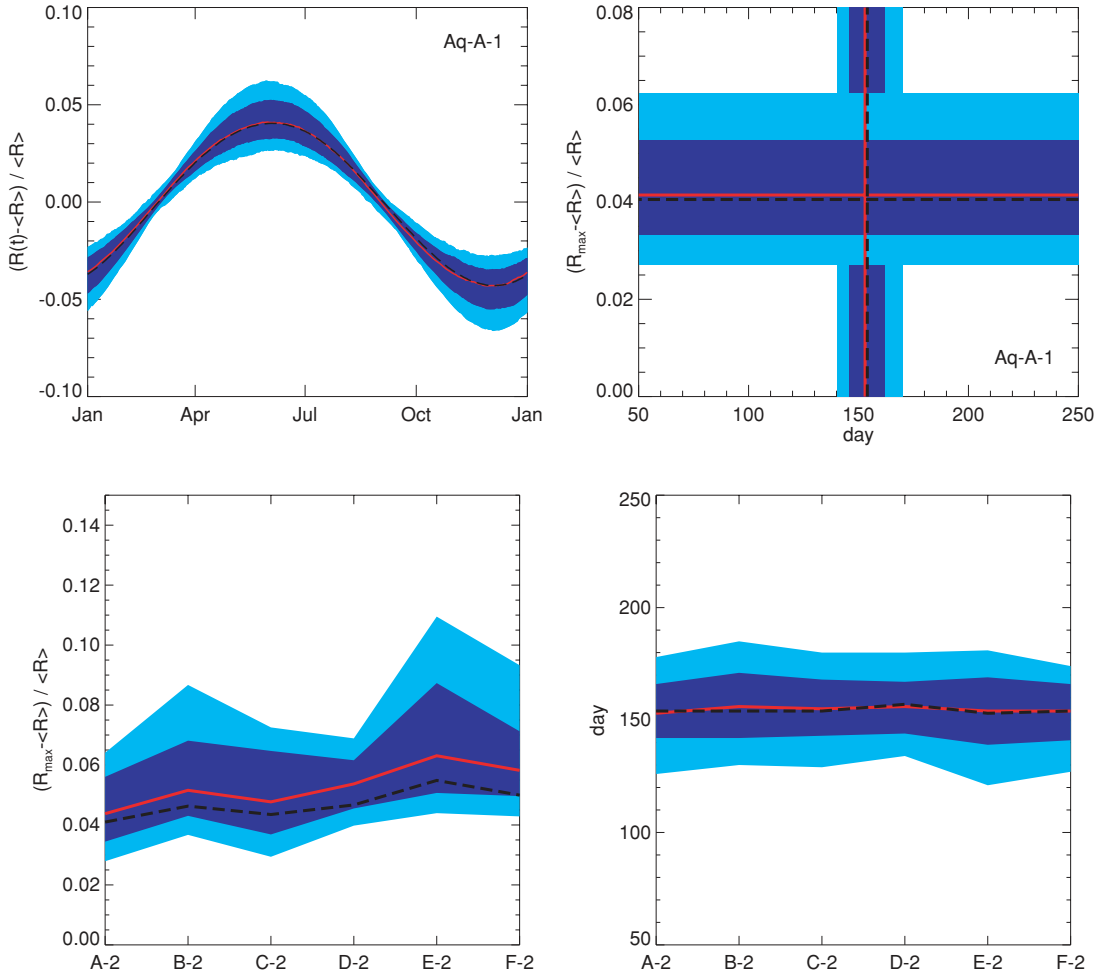

Figure 13. Top panels: annual modulation for all 2 kpc boxes with halocentric distance between 7 and 9 kpc in halo Aq-A-1 assuming $v_{\rm min} = 300\,{\rm km\,s^{-1}}$. The left plot shows how the dimensionless recoil rate $[R(t) - \langle R\rangle]/\langle R\rangle$ changes over the year. The right plot shows the corresponding modulation parameter space defined by the peak day (x-axis) and maximum amplitude ($R_{\rm max} - \langle R\rangle)/\langle R\rangle$($y$-axis). Bottom panels: modulation parameters for the local 2 kpc boxes of all level-2 resolution haloes. There is no clear trend visible in the day of maximum behaviour over the halo sample. On the other hand, the median amplitude in all boxes is higher than expected based on the Gaussian sample for $v_{\rm min} = 300\,{\rm km\,s^{-1}}$. The line and contour scheme is the same as in Fig. 2.

characteristic way from the Gaussian distributions as shown in Section 4. The deviations in the recoil spectra are typically highest at high energies.

10 per cent deviations in the recoil spectra are larger than the typical deviations expected due to the annual modulation. Therefore, these deviations from the Gaussian model can also influence the annual modulation signal. In Fig. 13 (top row), we plot the dimensionless recoil rate $[R(t) - \langle R\rangle]/\langle R\rangle$ of all local 2 kpc boxes at ∼8 kpc from the centre of Aq-A-1 (left-hand panel), where $\langle R\rangle$ is the annual mean recoil. We have assumed $v_{\rm min} = 300\,{\rm km\,s^{-1}}$ for all plots in this figure. The maximum can clearly be seen around the month of June. The plot on the right-hand panel in Fig. 13 shows the modulation parameter space that we define by the day of maximum amplitude (x-axis) and the maximum modulation amplitude of the recoil rate over the year defined as $(R_{\rm max} - \langle R\rangle)/\langle R\rangle$ (y-axis). The bottom row of Fig. 13 shows the maximum amplitude (left-hand panel) and day of maximum (right-hand panel) for all level-2 haloes (solid red) and the corresponding best-fitting multivariate Gaussian model (dashed black).

Comparing the Gaussian median values to the box median values one can see that the day of maximum amplitude does not deviate significantly from that predicted for a multivariate Gaussian; in particular, there is no clear trend visible over the halo sample. On the other hand, the median amplitude in all haloes is slightly higher than expected based on the Gaussian sample for $v_{\rm min} = 300\,{\rm km\,s^{-1}}$.

The amplitude differences for various $v_{\rm min}$ values are shown in Fig. 14. Here, we calculated the maximum amplitude and day of maximum for different $v_{\rm min}$ values for all level-2 haloes. The amplitude plot (top panel) shows the difference between the maximum relative modulation amplitude observed in the simulation and that expected for the best-fitting multivariate Gaussian model. The maximum amplitude $v_{\rm min}$-dependence is similar for the six haloes. Since only the velocity distribution enters into the recoil calculation, this similarity is due to the fact that deviations of the halo velocity distribution from the Gaussian model are also quite similar for all six haloes. The bottom plot of Fig. 14 shows the day of maximum amplitude is well predicted by the multivariate Gaussian for all haloes. The sharp transition in the day of maximum is due to the well-known phase-reversal effect (Primack, Seckel & Sadoulet 1988). We checked that the subhalo-dominated box in Aq-B-2, where by chance about 60 per cent of the box mass is in a single subhalo, leads to a very different modulation signal. The day of maximum in that case shifts about 100 d from the Gaussian distribution. We note that although the subhalo mass fraction in this particular box is high, the subhalo volume fraction is tiny, so even within this box, almost all observers would see the smooth regular signal.

Although most of the direct experiments currently search for WIMPs, the axion provides another promising candidate for CDM. It arises from the Peccei–Quinn solution to the strong charge-parity (CP) problem. One axion detection scheme is based on using the axion-electromagnetic coupling to induce resonant conversions of axions to photons in the microwave frequency range. Galactic axions have non-relativistic velocities ($\beta = v/c \sim 10^{-3}$) and the axion-to-photon conversion process conserves energy, so that the frequency of converted photons can be written as

$$\nu_{\rm a} = \nu_{\rm a}^0 + \Delta\nu_{\rm a} = 241.8\left(\frac{m_{\rm a}}{1\,\mu{\rm eV}/c^2}\right)\left(1 + \frac{1}{2}\beta^2\right)\,{\rm MHz}, \qquad (10)$$

where $m_{\rm a}$ is the axion mass that lies between 10^{-6} and $10^{-3}\,{\rm eV}/c^2$. 5 μeV axions would therefore convert into $\nu_{\rm a}^0 \cong 1200$ MHz photons with an upward spread of $\Delta \sim \cong 2$ kHz due to their kinetic energy. An advantage of axion detection compared to WIMP searches is the fact that it is directly sensitive to the energy rather than to the integral over the velocity distribution. The power P developed in the axion search cavity due to resonant axion-photon conversion can be written as (Sikivie 1983)

$$P = \mathcal{P}\rho_{\rm a}(\nu_{\rm cavity}), \qquad (11)$$

where $\mathcal{P}$ encapsulates the experimental properties (cavity volume, magnetic field and quality factor) and particle physics properties (model-dependent coupling parameter and axion mass). The only astrophysical input is the local density $\rho_{\rm a}(\nu_{\rm cavity})$ of axions with energies corresponding to the cavity frequency. For simplicity, we set $\mathcal{P} = 1$. We can produce axion spectra from our simulations by taking a local volume element (a box) and computing the distribution of kinetic energies K of the particles found in this location. The number of particles with a given K is then directly proportional to $\rho_{\rm a}$ at this frequency, and so to the power in the frequency bin.

To make the results independent of axion mass and other experimental properties, we present histograms of β^2 normalized to 1. For a given axion mass $m_{\rm a}$ (in $\mu{\rm eV}/c^2$), the x-axis must be transformed according to $x \rightarrow 241.8\ {\rm m_a}(1 + 1/2x)$ to get the corresponding frequencies in MHz.

A long-running axion search experiment is Axion Dark Matter Experiment (ADMX) at Lawrence Livermore National Laboratory (LLNL) (Hagmann et al. 1996). It has channels at medium and high resolution. The latter has a frequency resolution of about 0.02 Hz. For $\nu_{\rm a}^0 = 500$ MHz and an axion velocity of $v = 200\,{\rm km\,s^{-1}}$, this translates into a velocity width of only $0.018\ {\rm km\ s^{-1}}$.[2] Our numerical resolution prevents us from predicting the behaviour on such small scales. For wider bin searches and especially for the medium-resolution channel (125 Hz corresponding to a typical velocity spread of about $100\ {\rm km\ s^{-1}}$), we can, however, make reliable predictions by binning particles with respect to β^2.

In Fig. 15, we show axion spectra for all level-2 haloes.[3] In a broad sense, the spectra obtained from our simulations look similar to those of multivariate Gaussian models. However, there are a number of differences. For example, the peak power is shifted to lower frequencies. The Gaussian distribution is also a poor description of the spectrum at low frequencies. In all haloes, the power at low and high frequencies is higher then expected from a multivariate Gaussian model. This effect is quite small for high frequencies but very significant for low frequencies. The higher power at low frequencies can be understood from the velocity distributions in Fig. 4. In Aq-B-2, the subhalo-dominated box that was seen in Fig. 4 is clearly visible as a peak in the power spectrum at high frequency. The bumps in the velocity distribution also result in quite significant features in the axion spectra that might be visible in the medium-resolution channel given enough signal-to-noise ratio.

7 CONCLUSION

We have characterized the local phase-space distribution of DM using the recently published ultrahigh-resolution simulations of

[2] For non-relativistic motion, we can write $dv = (c^2/v)\,(dv/\nu_{\rm a}^0)$.

[3] We neglect the effects of the Earth's motion when constructing the spectra since here our focus is on the general spectral shape. This motion typically leads to a shift of about 100 Hz due to annual modulation and a daily shift of about 1 Hz due to the Earth's rotation (Duffy et al. 2005).

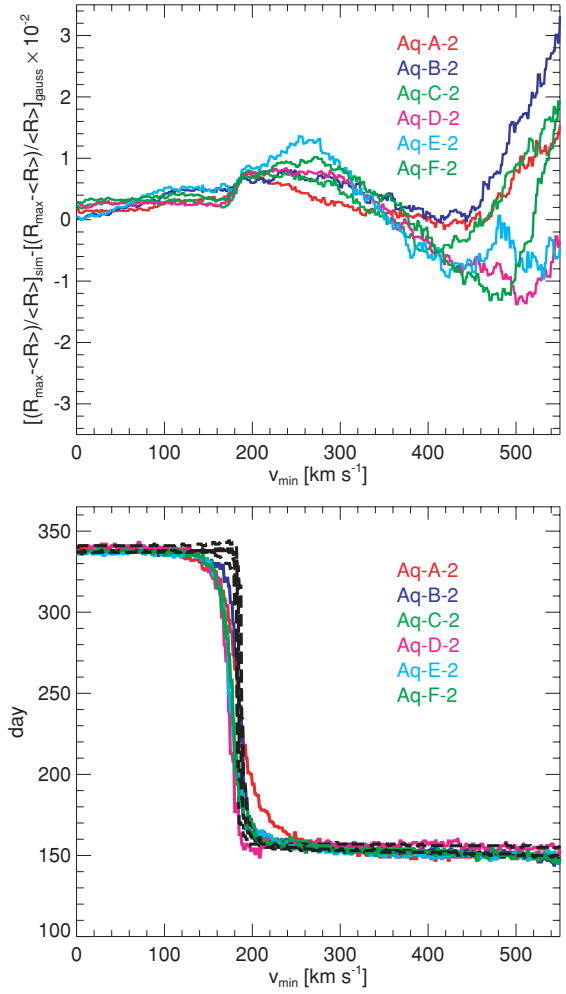

Figure 14. Top panel: median recoil rate amplitude for all 2 kpc boxes with halocentric distance between 7 and 9 kpc for all level-2 haloes. The plot shows the difference between the relative maximum modulation amplitude observed in the simulation and that expected for the best-fitting multivariate Gaussian distribution. Bottom panel: median day of maximum amplitude for the same haloes (solid red) compared to their Gaussian predictions (dashed black). The day of maximum amplitude is the same for all boxes and well reproduced in the Gaussian model. The phase reversal can clearly be seen.

the Aquarius project. Our study provides new insights relevant to searches for the elusive CDM particles. This results from the unprecedented resolution and convergence (in a dynamical sense) of our simulations, as well as from the fact that they provide a sample of six Milky Way like DM haloes.

We have measured the probability distribution function of the DM mass density between 6 and 12 kpc from the centre of the halo, finding it to be made up of two components: a truly smooth distribution which scatters around the mean on ellipsoidal shells by less than 5 per cent in all the haloes of our sample and a high-density tail associated with subhaloes. The smooth DM component dominates the local DM distribution. With 99.9 per cent confidence, we can say that the Sun lies in a region where the density departs from the mean on ellipsoidal shells by less than 15 per cent. Experimentalists can safely adopt smooth models to estimate the DM density near the Sun.

We find that the local velocity distribution is also expected to be very smooth, with no sign of massive streams or subhalo contributions. The standard assumption of a Maxwellian velocity distribution is not correct for our haloes, because the velocity distribution is clearly anisotropic. The velocity ellipsoid at each point aligns very well with the shape of the halo. A better fit to the simulations is given by a multivariate Gaussian. Even this description does not reproduce the exact shape of the distributions perfectly. In particular, the modulus of the velocity vector shows marked deviations from such model predictions. Velocity distributions in our six different haloes share common features with respect to the multivariate Gaussian model: the low-velocity region is more populated in the simulation; the peak of the simulation distribution is depressed compared to the Gaussian; at high velocities, there is typically an excess in the simulation distribution compared to the best-fitting multivariate Gaussian. Furthermore, the velocity distribution shows features which are stable in time, reproduced from place to place within a given halo, but differ between different haloes. These are related to the formation history of each individual halo.

The imprints in the modulus of the velocity vector reflect features in the energy distribution. We explicitly show that the mean phase-space density as a function of energy contains characteristic wiggles. The amplitude of these wiggles with respect to the average mean phase-space density distribution of our sample of six haloes rises from high- to low-binding energies. After appropriate scaling, the most bound part of the mean phase-space density distribution looks very similar in all haloes, suggesting a (nearly) universal shape. The weakly bound part of the distribution, on the other hand, can deviate in any given halo by an order of magnitude from the mean.

We have used our simulations to predict detector signals for WIMP and axion searches. We find that WIMP recoil spectra can deviate about 10 per cent from the recoil rate expected from the best-fitting multivariate Gaussian model. The energy dependence of these deviations looks similar in all six haloes; especially, at higher binding energies. We find that the annual modulation signal peaks around the same day as expected from a multivariate Gaussian model with no clear trend over our halo sample for varying recoil velocity thresholds. The maximum recoil modulation amplitude, on the other hand, shows a clear threshold-dependent difference between the signal expected for a multivariate Gaussian model and that estimated from the simulation. We have also explored the expected signal for direct detection of axions. We find the axion spectra to be smooth without any sign of massive streams. The spectra show characteristic deviations from those predicted by a multivariate Gaussian model; the power at low and high frequencies is higher than expected. The most pronounced effect is that the spectra peak at lower frequencies than predicted. Since the frequencies in the axion detector are directly proportional to the kinetic energy of the axion particles, the bumps in the DM velocity and energy distributions are also clearly visible in the axion spectra. All the effects on the various detector signals are driven by differences in the velocity distribution. Individual subhaloes or streams do not influence the detector signals however, since they are subdominant by a large factor in all six haloes.

Our study shows that, once direct DM detection has become routine, the characterization of the DM energy distribution will provide unique insights into the assembly history of the Milky Way halo. In the next decade, a new field may emerge, that of 'DM astronomy'.

ACKNOWLEDGMENTS

The simulations for the Aquarius Project were carried out at the Leibniz Computing Center, Garching, Germany, at the Computing

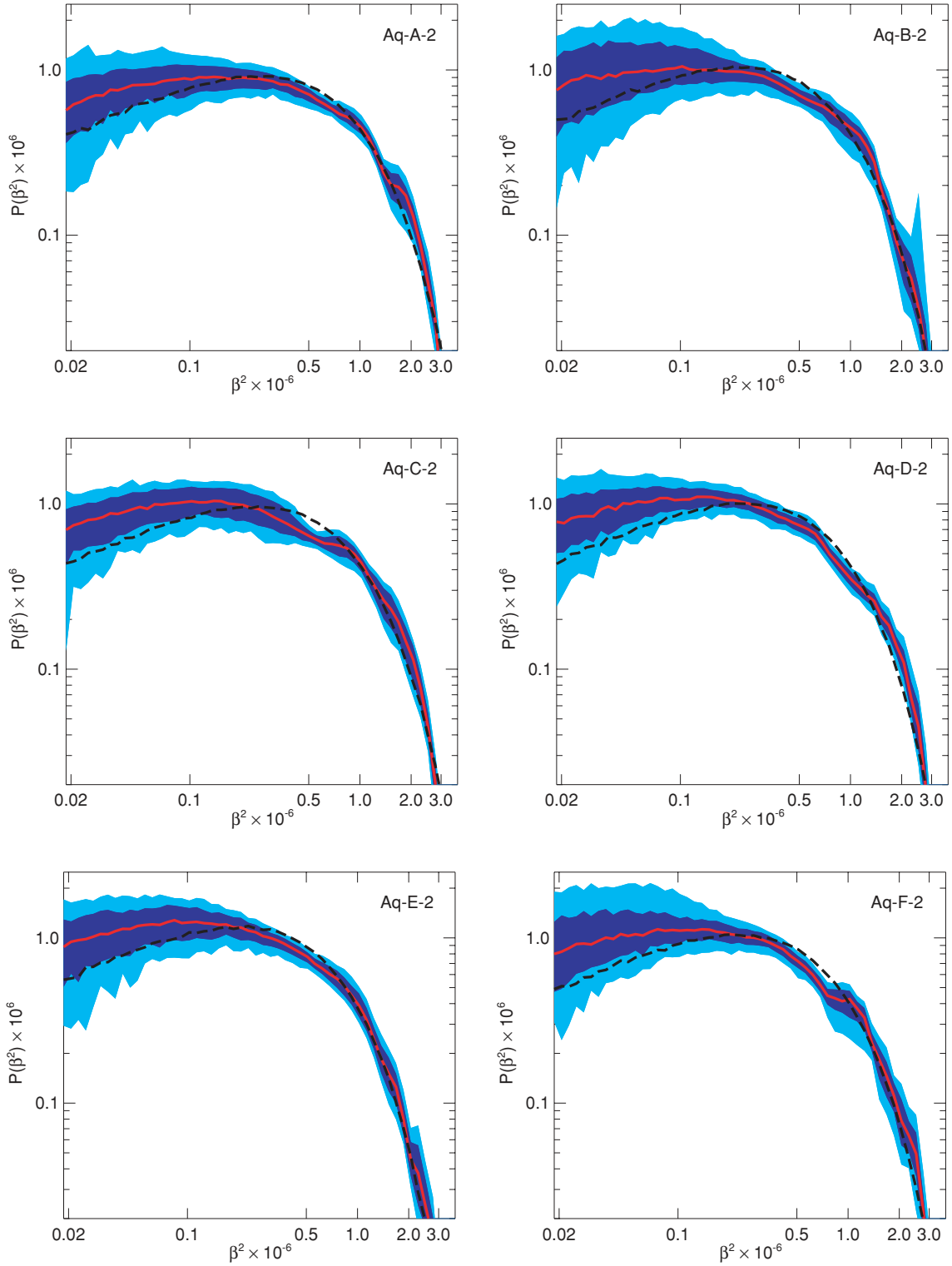

Figure 15. Axion spectra of level-2 haloes for all 2 kpc boxes with halocentric distance between 7 and 9 kpc. Rescaling the x-axis according to $x \rightarrow 241.8\ m_a(1 + 1/2\ x)$ for an axion mass m_a in μeV yields the x-axis in MHz. The y-axis is proportional to the power P developed in the detector cavity. Therefore, the panels show the predicted frequency spectra expected for an axion search experiment like ADMX. These spectra can be reasonably described by a multivariate Gaussian but significant differences remain. The maximum in the power is at lower frequencies in the simulation than in the Gaussian model. The bumps already found in the velocity and energy distribution are clearly visible in these spectra. In all haloes, the power at low frequencies is higher than expected from the Gaussian model. The line and contour scheme are the same as in Fig. 2.

Centre of the Max-Planck-Society in Garching, at the Institute for Computational Cosmology in Durham and on the 'STELLA' supercomputer of the LOFAR experiment at the University of Groningen. The analysis for this work was mainly done on the OPA and VIP computing clusters at the Computing Centre of the Max-Planck-Society in Garching. MV acknowledges the Kapteyn Astronomical Institute in Groningen for a productive atmosphere where most of this work was done. MV thanks Anne Green for helpful discussions. AH acknowledges financial support from NOVA and NWO. This research was supported by the DFG cluster of excellence 'Origin and Structure of the Universe'. We acknowledge support from the STFC rolling grant to the ICC; CSF acknowledges a Royal Society Wolfson Research Merit award.

REFERENCES

Bernabei R. et al., 2007, in Sissakian A., Kozlov G., Kolganova E., eds, Proc. 33rd International Conference, High Energy Physics: ICEP '06. World Scientific Press, Singapore, p. 214
Binney J., Merrifield M., 1998, Galactic Astronomy. Princeton Univ. Press, Princeton, NJ
Diemand J., Kuhlen M., Madau P., Zemp M., Moore B., Potter D., Stadel J., 2008, Nat, 454, 735
Drukier A. K., Freese K., Spergel D. N., 1986, Phys. Rev. D, 33, 3495
Duffy L. et al., 2005, Phys. Rev. Lett., 95, 091304
Ellis J., Engvist K., Nanopoulos D. V., Olive K. A., Srednicki M., 1984, NASA STI/Recon Technical Report N, 85, 26469
Freese K., Frieman J., Gould A., 1988, Phys. Rev. D, 37, 3388
Gehrels N., Michelson P., 1999, Astropart. Phys., 11, 277
Gelmini G. B., 2006, J. Phys. Conf. Ser., 39, 166
Gnedin O. Y., Kravtsov A. V., Klypin A. A., Nagai D., 2004, ApJ, 616, 16
Gondolo P., Gelmini G., 2005, Phys. Rev. D, 71, 123520
Green A. M., 2001, Phys. Rev. D, 63, 043005
Gunn J. E., Lee B. W., Lerche I., Schramm D. N., Steigman G., 1978, ApJ, 223, 1015
Hagmann C. et al., 1996, Nucl. Phys., 51, 209
Helmi A., 2004, ApJ, 610, L97
Helmi A., White S. D., Springel V., 2002, Phys. Rev. D, 66, 063502
Helmi A., White S. D. M., Springel V., 2003, MNRAS, 339, 834
Jungman G., Kamionkowski M., Griest K., 1996, Phys. Rep., 267, 195
Kamionkowski M., Koushiappas S. M., 2008, Phys. Rev. D, 77, 103509
Kazantzidis S., Kravtsov A. V., Zentner A. R., Allgood B., Nagai D., Moore B., 2004, ApJ, 611, L73
Kerr F. J., Lynden-Bell D., 1986, MNRAS, 221, 1023
Komatsu E. et al., 2009, ApJS, 180, 330
Law D. R., Johnston K. V., Majewski S. R., 2005, ApJ, 619, 807
Lee B. W., Weinberg S., 1977, Phys. Rev. Lett., 39, 165
Lewin J. D., Smith P. F., 1996, Astropart. Phys., 6, 87
Moore B., Calcáneo-Roldán C., Stadel J., Quinn T., Lake G., Ghigna S., Governato F., 2001, Phys. Rev. D, 64, 063508
Peccei R. D., Quinn H. R., 1977a, Phys. Rev. D, 16, 1791
Peccei R. D., Quinn H. R., 1977b, Phys. Rev. Lett., 38, 1440
Peebles P. J. E., 1982, ApJ, 263, L1
Primack J. R., Seckel D., Sadoulet B., 1988, Annu. Rev. Nucl. Part. Sci., 38, 751
Savage C., Gondolo P., Freese K., 2004, Phys. Rev. D, 70, 123513
Savage C., Freese K., Gondolo P., 2006, Phys. Rev. D, 74, 043531
Sikivie P., 1983, Phys. Rev. Lett., 51, 1415
Sikivie P., 1985, Phys. Rev. D, 32, 2988
Sikivie P., Tkachev I. I., Wang Y., 1995, Phys. Rev. Lett., 75, 2911
Spergel D. N. et al., 2003, ApJS, 148, 175
Springel V. et al., 2008a, MNRAS, 391, 1685
Springel V. et al., 2008b, Nat, 456, 73
Stadel J., Potter D., Moore B., Diemand J., Madau P., Zemp M., Kuhlen M., Quilis V., 2008, preprint
Stiff D., Widrow L. M., 2003, Phys. Rev. Lett., 90, 211301
Stiff D., Widrow L. M., Frieman J., 2001, Phys. Rev. D, 64, 083516
Ullio P., Kamionkowski M., 2001, J. High Energy Phys., 3, 49
Vogelsberger M., White S. D. M., Helmi A., Springel V., 2008, MNRAS, 385, 236
Weinberg S., 1978, Phys. Rev. Lett., 40, 223
Wilczek F., 1978, Phys. Rev. Lett., 40, 279
Zemp M., Diemand J., Kuhlen M., Madau P., Moore B., Potter D., Stadel J., Widrow L., 2009, MNRAS, in press (arXiv:0812.2033)
Zwicky F., 1933, Helv. Phys. Acta, 6, 110

This paper has been typeset from a TEX/LATEX file prepared by the author.